# Near-field radiative heat transfer between shifted graphene gratings

Minggang Luo, Youssef Jeyar, Brahim Guizal, Mauro Antezza

# Near-field radiative heat transfer between shifted graphene gratings

Minggang Luo [1,*] Youssef Jeyar [1] Brahim Guizal [1] and Mauro Antezza [1,2,†]
[1] *Laboratoire Charles Coulomb (L2C), UMR 5221 CNRS-Université de Montpellier, F-34095 Montpellier, France*
[2] *Institut Universitaire de France, 1 rue Descartes, Paris Cedex 05, F-75231, France*

(Received 25 January 2024; revised 24 April 2024; accepted 2 May 2024; published 28 May 2024)

We examine the near-field radiative heat transfer between finite-thickness planar fused silica slabs covered with graphene gratings, through the utilization of the Fourier modal method augmented with local basis functions (FMM-LBF), with a focus on the lateral shift effect (LSE). To do so, we propose and validate a minor modification of the FMM-LBF theory to account for the lateral shift. This approach goes far beyond the effective medium approximation, which cannot account for the lateral shift. We show that the heat flux can exhibit significant oscillations with the lateral shift, and at short separation, it can experience up to a 60–70% reduction compared with the aligned case. Such an LSE is found to be sensitive to the geometric factor $d/D$ (separation distance to grating period ratio). When $d/D > 1$ (realized through large separation or small grating period), the two graphene gratings see each other as an effective whole rather than in detail, and thus, the LSE on heat transfer becomes less important. Therefore, we can clearly distinguish two asymptotic regimes for radiative heat transfer: the LSE regime, where a significant LSE is observed, and the non-LSE regime, where this effect is negligible. Furthermore, regardless of the lateral shift, the radiative heat flux shows a nonmonotonic dependence on the graphene chemical potential. That is, we can get an optimal radiative heat flux (peaking at ∼0.3 eV chemical potential) by modulating the chemical potential *in situ*. This paper has the potential to unveil avenues for harnessing the LSE on radiative heat transfer in graphene-based nanodevices.

DOI: 10.1103/PhysRevB.109.195431

## I. INTRODUCTION

Recently, interest has been growing in near-field radiative heat transfer (NFRHT), motivated by both fundamental explorations and practical applications. When the separation distance is comparable with or smaller than the thermal wavelength $\lambda_T = \hbar c/k_B T$, the radiative heat flux can exceed the Planckian black-body limit by several orders of magnitude [1,2], due to the near-field effects (e.g., photon tunneling) [3–6]. NFRHT has been extensively investigated theoretically for many different geometric configurations [7–19], some of which have been confirmed by pioneering experimental works [20–29]. Particularly, when grating structures are involved, they can lead to important enhancement of NFRHT due to the excitation of high-order diffraction channels [30–32]. Additionally, owing to the special optical properties of graphene, planar graphene-sheet-involved structures exhibit many behaviors in the radiative heat transfer modulation [33–42]. It would be interesting to know whether the combined richness of the grating geometry and the special dielectric features of graphene could lead to some other behaviors in NFRHT manipulation that cannot be achieved with conventional materials.

Radiative energy transfer between graphene grating-based structures [43–45] has recently been investigated, where patterning the graphene sheets has been found to open more energy transfer channels. All of these works consider two perfectly aligned and identically patterned graphene structures. The effect of twisted grating has also been investigated [46–48]. Still, the effect of a lateral shift between the two parallel gratings remains unexplored. Introducing a lateral shift will allow a modulation of NFRHT, keeping the separation distance constant. It is worth stressing that the effective medium theory (EMT), which is often used to study NFRHT between substrate-supported graphene strips [49], treats the graphene grating as an effective whole and thus cannot account for the lateral shift effect (LSE). The study of a shifted configuration needs a more accurate numerical method to treat the electromagnetic wave scattering by the gratings.

In this paper, we investigate the effect of a lateral shift on NFRHT. We will consider planar fused silica slabs coated with graphene gratings (see Fig. 1). Concerning the numerical investigations, we will use a more accurate method: the Fourier modal method equipped with local basis functions (FMM-LBF), which is particularly efficient for one-dimensional strip gratings [50–53]. Such a method does not use any approximations other than the classical ones (harmonic plane-wave expansion, linear homogeneous and isotropic materials, etc.) in the solution of Maxwell's equations. The restriction, if there is one, is the truncation necessary for the numerical implementation. There is no such restriction on the wavelength-to-period ratio like the one we have with the EMT. To consider this lateral shift, one can either include it by directly applying the translation to the scattering operator (of nontranslated objects) or by including it in the construction of the scattering operators themselves. In our computations, we checked the equivalence of these two approaches.

*minggang.luo@umontpellier.fr
†mauro.antezza@umontpellier.fr

 

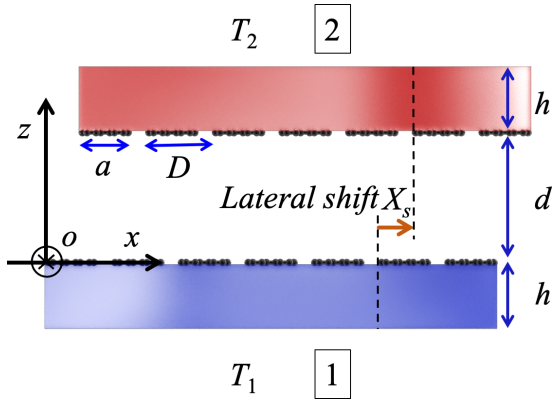


FIG. 1. Structure diagram of the supported graphene gratings considering relative lateral shift $X_s$

This paper is organized as follows: In Sec. II, the physical model of the planar fused silica slabs covered with graphene gratings with a relative lateral shift and the theoretical models of the scattering approach for radiative heat transfer are presented. In Sec. III, the effects of influencing factors (e.g., grating period, chemical potential, and filling fraction) on the lateral shift mediated NFRHT are analyzed, and asymptotic regimes of the LSE are also proposed.

## II. THEORETICAL MODELS

The physical system is shown in Fig. 1. We investigate NFRHT between bodies 1 and 2. The relative lateral displacement between the two graphene strips along the $x$ axis is $X_s$. When $X_s = 0$, the two graphene gratings are perfectly aligned, and NFRHT, in this case, has recently been investigated (please refer to our recent work for more details [45]).

In the following, we will denote by $D$ the graphene grating period, by $a$ the width of a single graphene strip, by $h$ the common thickness of the planar slabs, and by $d$ the separation distance between the two gratings. Bodies 1 and 2 are considered at fixed temperatures $T_1$ and $T_2$, respectively, while the environment is at the same temperature as body 1. The electromagnetic properties of graphene are considered through its conductivity $\sigma_g$, which depends on the temperature $T$ and chemical potential $\mu$. It is the sum of intraband and interband contributions ($\sigma_g = \sigma_{\text{intra}} + \sigma_{\text{inter}}$) given by [37,54–56]

$$\sigma_{\text{intra}} = \frac{i}{\omega + i/\tau}\frac{2e^2 k_B T}{\pi\hbar^2}\ln\left[2\cosh\left(\frac{\mu}{2k_B T}\right)\right], \tag{1}$$

and

$$\sigma_{\text{inter}} = \frac{e^2}{4\hbar}\left[G\left(\frac{\hbar\omega}{2}\right) + i\frac{4\hbar\omega}{\pi}\int_0^{+\infty}\frac{G(\xi) - G(\hbar\omega/2)}{(\hbar\omega)^2 - 4\xi^2}d\xi\right], \tag{2}$$

where $e$ is the electron charge, $\tau$ the relaxation time (we use $\tau = 10^{-13}$ s), and $G(\xi) = \sinh(\xi/k_B T)/[\cosh(\mu/k_B T) + \cosh(\xi/k_B T)]$.

The net power flux $\varphi$ received by body 1 (energy per unit surface and time) can be defined as [57,58]

$$\varphi = \sum_p \int \frac{d^2\mathbf{k}}{(2\pi)^2}\int_0^{+\infty}[\Theta(\omega, T_2) - \Theta(\omega, T_1)] \times \frac{d\omega}{2\pi}\langle p, \mathbf{k}|\mathcal{O}|p, \mathbf{k}\rangle, \tag{3}$$

where $p$ is the polarization index, $p = 1, 2$ correspond to transverse electric (TE) and transverse magnetic (TM) polarization modes, respectively, $\Theta(\omega, T) = \hbar\omega/[\exp(\hbar\omega/k_B T) - 1]$ is the mean energy of the Planck oscillator, $\hbar$ is the reduced Planck constant, $\omega$ is the angular frequency, $k_B$ is the Boltzmann constant, and $\mathbf{k} = (k_x, k_y)$, $k_x$ and $k_y$ being the wave vectors in the standard $(x, y, z)$ Cartesian coordinates system. The transmission operator $\mathcal{O}$ in the (TE, TM) basis is given by [58]

$$\mathcal{O} = U^{(2,1)}\left\{f_{-1}[\mathcal{R}^{(2)-}] - \mathcal{T}^{(2)-}\mathcal{P}_{-1}^{(\text{pw})}\mathcal{T}^{(2)-\dagger}\right\} \times U^{(2,1)\dagger}\left\{f_1[\mathcal{R}^{(1)+}] - \mathcal{T}^{(1)-\dagger}\mathcal{P}_1^{(\text{pw})}\mathcal{T}^{(1)-}\right\}, \tag{4}$$

where $U^{(2,1)} = [1 - \mathcal{R}^{(2)-}\mathcal{R}^{(1)+}]^{-1}$, $\mathcal{R}^{(1)+}$ and $\mathcal{R}^{(2)-}$ [$\mathcal{T}^{(1)-}$ and $\mathcal{T}^{(2)-}$] are the reflection operators (transmission operators) of gratings 1 and 2 in the (TE, TM) basis, $\dagger$ stands for the conjugation operation, and the $\pm$ superscripts in the reflection and transmission coefficients correspond to the propagation direction with respect to the $z$ axis. Here, $\langle p, \mathbf{k}|\mathcal{P}_\zeta^{(\text{pw/ew})}|p', \mathbf{k}'\rangle = k_z^\zeta\langle p, \mathbf{k}|\prod^{(\text{pw/ew})}|p', \mathbf{k}'\rangle$, $k_z = \sqrt{k_0^2 - \mathbf{k}^2}$, $k_0 = \omega/c$, $\prod^{(\text{pw})}$ [$\prod^{(\text{ew})}$] is the projector on the propagative (evanescent) sector, and the auxiliary function $f_\zeta(\mathcal{R})$ is given by [57,58]

$$f_\zeta(\mathcal{R}) = \begin{cases}\mathcal{P}_{-1}^{(\text{pw})} - \mathcal{R}\mathcal{P}_{-1}^{(\text{pw})}\mathcal{R}^\dagger + \mathcal{R}\mathcal{P}_{-1}^{(\text{ew})} - \mathcal{P}_{-1}^{(\text{ew})}\mathcal{R}^\dagger, & \zeta = -1,\\ \mathcal{P}_1^{(\text{pw})} - \mathcal{R}^\dagger\mathcal{P}_1^{(\text{pw})}\mathcal{R} + \mathcal{R}^\dagger\mathcal{P}_1^{(\text{ew})} - \mathcal{P}_1^{(\text{ew})}\mathcal{R}, & \zeta = 1.\end{cases} \tag{5}$$

According to Ref. [31], the periodicity along the $x$ axis makes it natural to replace the mode variable $k_x$ with $k_{xn} = k_x + n\frac{2\pi}{D}$, and $k_z$ becomes $k_{zn} = \sqrt{k_0^2 - k_{xn}^2 - k_y^2}$, where $n \in \mathbb{Z}$, $k_x$ is in the first Brillouin zone $(-\frac{\pi}{D}, \frac{\pi}{D})$, and $k_y \in \mathbb{R}$.

The reflection and transmission operators $\mathcal{R}^{(1)+}$, $\mathcal{R}^{(2)-}$, $\mathcal{T}^{(1)-}$, and $\mathcal{T}^{(2)-}$, needed for our calculations, are obtained from the operators $\mathcal{R}$ and $\mathcal{T}$ corresponding to the reference structure shown in Fig. 2 and whose derivation is detailed in the Appendix.

Body 1 has no lateral shift, i.e., $X_s = 0$. Then $\mathcal{R}^{(1)+}$ and $\mathcal{T}^{(1)-}$ at the interface $z = 0$ and with no lateral shift $X_s = 0$ (see Fig. 1) can be obtained directly from the known $\mathcal{R}^-$ and $\mathcal{T}^+$ by using the following relations [31,45]:

$$\langle p, \mathbf{k}, n|\mathcal{R}^{(1)+}(\omega)|p', \mathbf{k}', n'\rangle = \begin{cases} \langle p, \mathbf{k}, n|\mathcal{R}^{-}(\omega)|p, \mathbf{k}', n'\rangle, & p = p', \\ -\langle p, \mathbf{k}, n|\mathcal{R}^{-}(\omega)|p', \mathbf{k}', n'\rangle, & p \neq p', \end{cases} \tag{6}$$

and

$$\langle p, \mathbf{k}, n|\mathcal{T}^{(1)-}(\omega)|p', \mathbf{k}', n'\rangle = \begin{cases} \langle p, \mathbf{k}, n|\mathcal{T}^{+}(\omega)|p, \mathbf{k}', n'\rangle, & p = p' \\ -\langle p, \mathbf{k}, n|\mathcal{T}^{+}(\omega)|p', \mathbf{k}', n'\rangle, & p \neq p'. \end{cases} \tag{7}$$

As for body 2, there is not only a lateral shift $X_s$ but an interface translation to $z = d$ (see Fig. 1). To consider these two kinds of translation and obtain $\mathcal{R}^{(2)-}$ and $\mathcal{T}^{(2)-}$, one can consider two methods. The first one consists of directly applying appropriate translation operators to the scattering operators. This approach has been discussed, in detail, in a previous work [58] from which we take the results giving $\mathcal{R}^{(2)-}$ and $\mathcal{T}^{(2)-}$ in terms of $\mathcal{R}^-$ and $\mathcal{T}^-$:

$$\begin{aligned} \langle p, \mathbf{k}, n|\mathcal{R}^{(2)-}(\omega)|p', \mathbf{k}', n'\rangle &= \exp[i(k'_{xn'} - k_{xn})X_s] \exp[i(k_{zn} + k'_{zn'})d]\langle p, \mathbf{k}, n|\mathcal{R}^{-}(\omega)|p', \mathbf{k}', n'\rangle, \\ \langle p, \mathbf{k}, n|\mathcal{T}^{(2)-}(\omega)|p', \mathbf{k}', n'\rangle &= \exp[i(k'_{xn'} - k_{xn})X_s] \exp[i(k_{zn} - k'_{zn'})d]\langle p, \mathbf{k}, n|\mathcal{T}^{-}(\omega)|p', \mathbf{k}', n'\rangle. \end{aligned} \tag{8}$$

In the first method, when using Eq. (8), $\mathcal{R}^-$ and $\mathcal{T}^-$ are calculated by fixing $X_s = 0$ since the effect of the lateral shift is already included by the factor phase $\exp[i(k'_{xn'} - k_{xn})X_s]$.

The second method, consists of incorporating the effect of the lateral shift directly into the computation of the scattering operators $\mathcal{R}^-$ and $\mathcal{T}^-$ with FMM-LBF (as given in the Appendix) and then only applying the normal translation operators $\exp[i(k_{zn} + k'_{zn'})d]$ and $\exp[i(k_{zn} - k'_{zn'})d]$ (as previously) in the $z$ direction.

It is important to stress that these two approaches are completely equivalent. A numerical verification of this is shown in Fig. 3, where we compute the radiative heat flux spectrum for the structure shown in Fig. 1, using the two methods (the different parameters are given in the caption). As can be seen in the figure, there is very good agreement between the two approaches, and a closer look at the data reveals that the results are identical to our working precision [see the inset of the figure for the $\sim$0 relative ratio of heat flux $(\varphi_{\omega,1} - \varphi_{\omega,2})/\varphi_{\omega,2}$ between the two methods]. Therefore, either of these methods can be used in the investigations to come.

## III. RESULTS AND DISCUSSION

In this section, we use the theoretical model outlined above to investigate NFRHT between the slabs of Fig. 1. Parametric investigations of influencing factors on NFRHT will be performed, and particular focus will be given to the asymptotic regimes for the LSE. In the following, bodies 1 and 2 are maintained at $T_1 = 290\,\mathrm{K}$ and $T_2 = 310\,\mathrm{K}$, respectively. We notice that the convergence of truncation order $N$ used in FMM-LBF is independent of the homogeneous media surrounding graphene and the conductivity itself. More precisely, this $N$ convergence depends on the ratio between the wavelength and the period of the grating. In our computations, given the interval of wavelengths considered, we found that $N = 30$ is enough to ensure the convergent results for the radiative heat flux (the relative error $<1\%$). The substrate thickness $h$ is fixed at 20 nm.

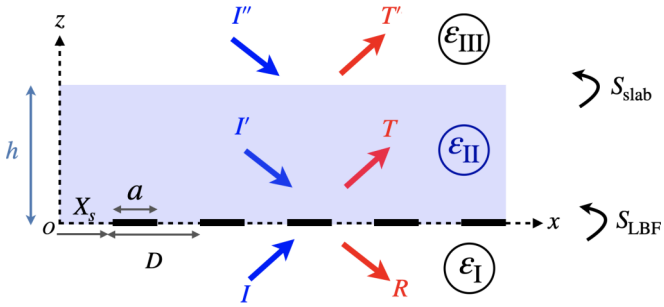


FIG. 2. Reference structure used in the computation of the different reflection and transmission operators.

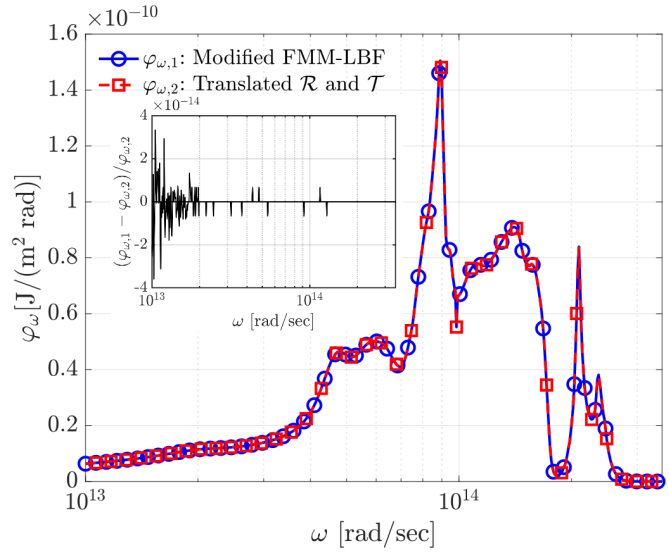


FIG. 3. The radiative heat flux spectrum of the configuration shown in Fig. 1 using $SiO_2$ slabs (whose optical data are taken from Ref. [59]), $\mu = 0.3\,\mathrm{eV}$, a lateral shift $X_s = 0.5\,\mu\mathrm{m}$ and a grating period $D = 2\,\mu\mathrm{m}$ at separation distance $d = 100$ nm, with $T_1 = 290\,\mathrm{K}$ and $T_2 = 310\,\mathrm{K}$, obtained by the two different approaches: (1) the modified FMM-LBF and (2) the translated scattering operators.

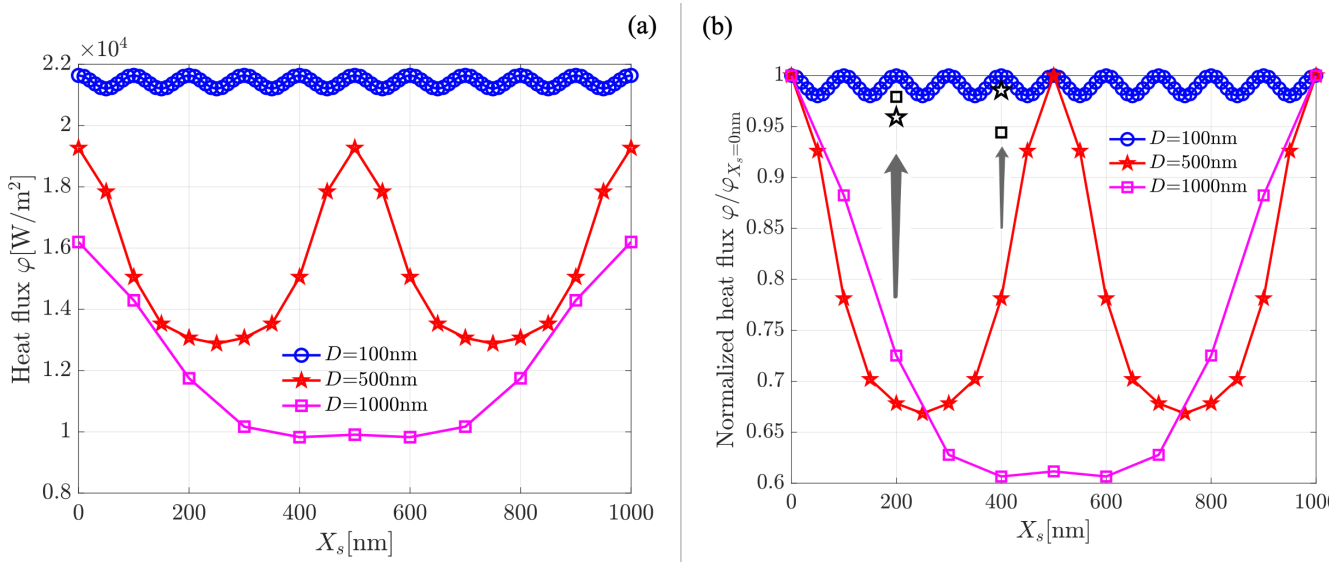


FIG. 4. Dependence of heat flux $\varphi$ and normalized heat flux $\varphi/\varphi(X_s = 0\,\text{nm})$ on the relative lateral shift $X_s$: (a) the absolute heat flux $\varphi$ and (b) ratio of the heat flux $\varphi$ to the heat flux at $X_s = 0$ nm. Three different periods are considered, $D = 100$, 500, and 1000 nm.

### A. Parametric investigation of influencing factors on lateral-shift-induced NFRHT: Grating period, chemical potential, and filling fraction

We consider three different influencing factors that may affect the effect of the relative lateral shift between the two gratings on its heat transfer: the grating period $D$, the chemical potential $\mu$ of graphene, and the filling fraction $f$. We start the parametric investigation with the grating period $D$. In Fig. 4(a), we show the dependence of heat flux $\varphi$ on the relative lateral shift $X_s$. Three different periods are considered, $D = 100$, 500, and 1000 nm, respectively. The other parameters are $f = 0.5$, $d = 100$ nm, and $\mu = 0.5\,\text{eV}$.

When shifting one of the gratings, we can observe a periodic oscillation of the radiative heat flux with the same spatial period as the grating itself. As shown in Fig. 4(a), for a fixed lateral shift $X_s$, the radiative heat flux decreases by ~30% when the period $D$ increases from 100 to 1000 nm. Additionally, the oscillation amplitude of the radiative heat flux induced by the lateral shift increases significantly with increasing period $D$. To show the change of the oscillation amplitude corresponding to different grating periods, we normalize the radiative heat flux $\varphi(X_s)$ by $\varphi(X_s = 0\,\text{nm})$ (i.e., the one without a lateral shift). The result is shown in Fig. 4(b). Lateral shift affects the heat transfer significantly. For the case where $D = 1000$ nm, the lateral shift can even result in 40% reduction of the heat flux, while for the case where $D = 100$ nm, the lateral shift can reduce it by only a few percent, which is negligible compared with that for the case of a large spatial period ($D = 1000$ and 500 nm). For a fixed separation distance $d$, the scattering details become more important when increasing the grating period $D$ (and thus the ratio $D/d$), causing the nanostructures to see each other in more detail. In such a situation, more accuracy is needed to account for the complexity of the nanostructures and be able to compare with experiments, while the EMT becomes completely invalid.

In our recent paper [53], when discussing the nonadditivity of the Casimir force (a kind of geometric effect) between two aligned graphene-grating-coated finite-size fused silica slabs (the same configuration as in this paper but with no lateral shift), we introduced a dimensionless parameter $d/D$ and proved its relevance to such a geometric effect. The effect of the relative lateral shift on NFRHT is also geometry related; therefore, we want to know if the dimensionless parameter $d/D$ is still pertinent in this case. The three curves in Fig. 4(b) correspond to a fixed separation distance $d = 100$ nm, where $d/D = 1$, 0.2, and 0.1 for the cases $D = 100$, 500, and 1000 nm, respectively. To verify the relevance of $d/D$ to the LSE, we performed additional calculations using the couples ($d = 500$ nm, $D = 500$ nm) and ($d = 1000$ nm, $D = 1000$ nm) to maintain $d/D = 1$ as for the case ($d = 100$ nm, $D = 100$ nm) already shown. Two lateral shift distances $X_s = 200$ and 400 nm are considered. The results are added in Fig. 4(b) and shown as the star and square symbols in black for periods $D = 500$ and 1000 nm, respectively. We see that they both move close to the $d = 100$ nm and $D = 100$ nm curve, confirming the relevance of the geometric factor $d/D$ and hence of the geometric nature of the effect. To further verify the relevance of $d/D$ to the LSE, the dependence of the amplitude ratio $\varphi_{X_s=0.5D}/\varphi_{X_s=0}$ on the period $D$ is shown in Fig. 5, where $d/D$ is fixed at 1. We observe that the ratio $\varphi_{X_s=0.5D}/\varphi_{X_s=0} \sim 1$ for the considered periods (100 nm $< D <$ 1000 nm). That is, maintaining $d/D = 1$ will bring a weak LSE compared with the significant LSE for the configurations ($d/D = 0.2$ and 0.1) in Fig. 4(b), which further confirms the relevance of the geometric factor $d/D$ to the LSE.

We then study the effect of the chemical potential $\mu$ of graphene on NFRHT. We show the dependence of heat flux $\varphi$ on the relative lateral shift $X_s$ in Fig. 6, considering different chemical potential values $\mu = 0$, 0.2, 0.4, 0.6, 0.8, and 1.0 eV, with $D = 1000$ nm, $f = 0.5$, and $d = 100$ nm. The upper body 2 is laterally shifted in the range of one full grating spatial period. At different Fermi levels, the LSE on NFRHT changes slightly. When the chemical potential is not too small (e.g., $\mu > 0.2\,\text{eV}$), when laterally shifting body 2,

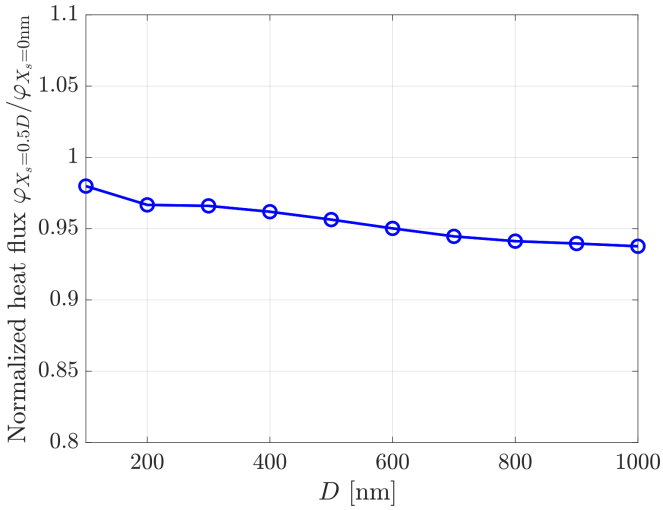


FIG. 5. Dependence of the ratio $\varphi_{X_s=0.5D}/\varphi_{X_s=0\,\text{nm}}$ on the period $D$. Here: $d/D = 1$, $f = 0.5$, $\mu = 0.5$ eV.

the radiative heat flux decreases to reach a valley, then keeps constant for a range of lateral shifts (forming a plateau), and finally increases to the same value as that without lateral shift, while for the chemical potentials $\mu = 0$ and 0.2 eV, radiative heat flux will decrease to reach the valley and then increase directly and go back to that of no lateral shift. Figure 6 also indirectly shows that the radiative heat flux is not monotonic with the chemical potential (this behavior will be studied in detail in Fig. 7). A natural question is whether we can obtain an optimal radiative heat flux by choosing an appropriate chemical potential $\mu$ for graphene gratings.

To answer the above question, we calculated the dependence of the radiative heat flux $\varphi$ on the chemical potential $\mu$ for different lateral shifts $X_s = 0$, 100, 200, 300, 400, and 500 nm, for $D = 1000$ nm, $f = 0.5$, and $d = 100$ nm. The results are reported in Fig. 7, where we see that, when increasing the chemical potential, the radiative heat flux increases at first to its peak and then decreases gradually for all considered lateral shift $X_s$ curves. For the considered separation $d$ and grating period $D$, the radiative heat flux appears to be optimal for $\mu$ at ∼0.25 eV.

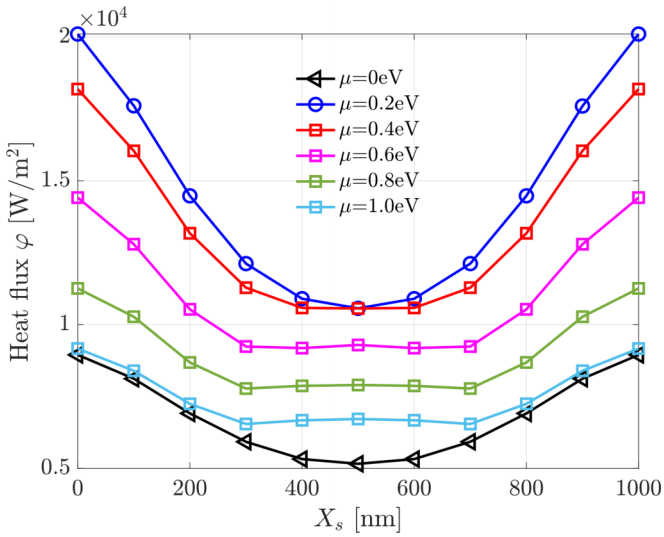


FIG. 6. Dependence of radiative heat flux $\varphi$ on the lateral shift $X_s$. The chemical potential $\mu = 0$, 0.2, 0.4, 0.6, 0.8, and 1.0 eV. The period $D = 1000$ nm, filling fraction $f = 0.5$, separation distance $d = 100$ nm.

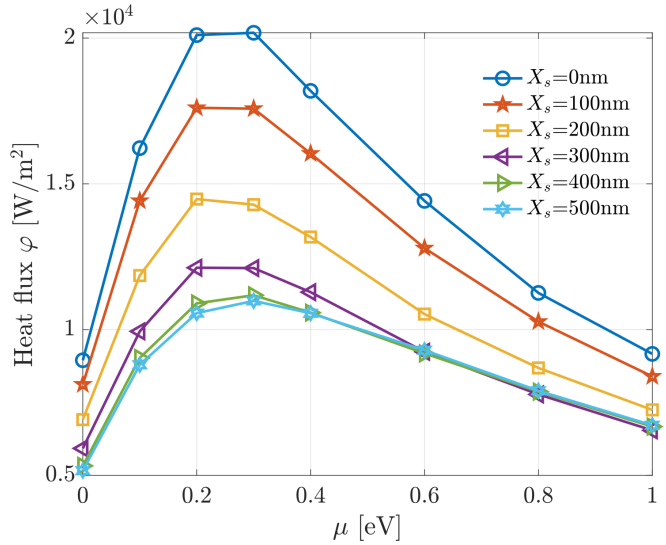


FIG. 7. Dependence of radiative heat flux $\varphi$ on the chemical potential $\mu$ of graphene. The lateral shift $X_s = 0$, 100, 200, 300, 400, and 500 nm, period $D = 1000$ nm, filling fraction $f = 0.5$, separation distance $d = 100$ nm.

Additionally, we study the effect of the filling fraction $f$ on NFRHT. We show the dependence of heat flux on the filling fraction in Fig. 8(a), where five different filling fractions are considered, $f = 0$, 0.2, 0.5, 0.8, and 1.0, with $d = 1000$ nm and $D = 1000$ nm. For $f = 0$ and 1.0, the configurations reduce to the bare/coated slab cases. As expected, the heat flux for these two cases is independent on the lateral shift. At a large separation (e.g., $d = 1000$ nm), adding a graphene sheet coating on the fused silica substrate (green right-facing triangle line) will significantly enhance the radiative heat flux as compared with the bare fused silica substrate (black left-facing triangle line), which is consistent with the observations in Refs. [33,45]. At short separations and without considering any lateral shift, as reported in our recent work [45], patterning graphene from a sheet to a grating can significantly enhance the heat flux. For the graphene grating coating case (e.g., $f = 0.8$), there are more accessible high-$k$ modes, while for the graphene sheet configuration ($f = 1.0$), the accessible wave vector region is relatively smaller than that of the graphene grating one. Consequently, the slabs coated with a graphene grating can facilitate a greater transfer of energy than the slabs coated with a graphene sheet. However, at large separations, the patterning method does not always work to enhance heat flux. As shown in Fig. 8(a), by comparing the curves for $f = 0.2$, 0.5, and 0.8 to the curve for $f = 1.0$, we can clearly see that, apart from the enhancement seen for $f = 0.8$, the patterning method fails to enhance the heat flux. Moreover, when laterally shifting the upper body 2 in the case $f = 0.8$, the heat flux will become less than that of the graphene sheet coating case ($f = 1.0$) (for $X_s \in [200, 800]$ nm).

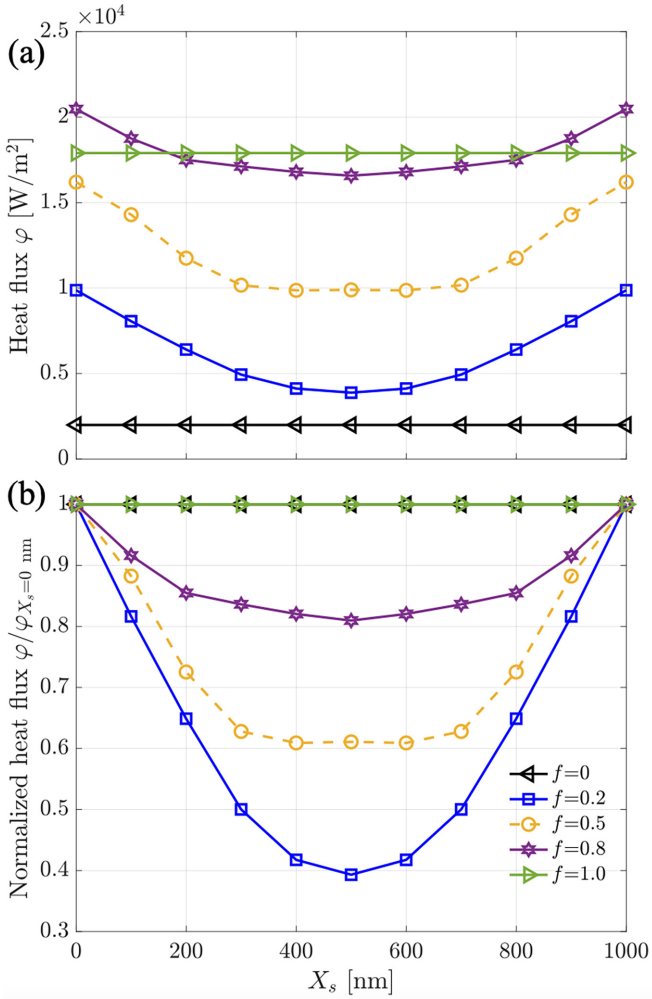


FIG. 8. Dependence of heat flux $\varphi$ and normalized heat flux $\varphi/\varphi\,(X_s = 0\,\text{nm})$ on the relative lateral shift $X_s$: (a) the absolute heat flux $\varphi$ and (b) ratio of the heat flux $\varphi$ to the heat flux at $X_s = 0$ nm. Five different filling fractions are considered, $f = 0$, 0.2, 0.5, 0.8, and 1.0, respectively. The separation distance $d = 100$ nm, grating period $D = 1000$ nm, chemical potential $\mu = 0.5$ eV.

In Fig. 8(b), we show the dependence of the ratio $\varphi(X_s)/\varphi(X_s = 0)$ on the filling fraction $f$. As expected, it is constant and equal to 1 for both $f = 0$ and 1. For the other filling fractions, this ratio decreases from 1 to a valley value and then increases back to 1. For a lateral shift ~500 nm, the heat flux can even experience up to 60% reduction when $f = 0.2$. In general, the minimal heat flux is at the half-period lateral shift ($X_s = 0.5D$). However, it is not always the case. For example, as shown in Fig. 4(b), the minimal heat flux is at $X_s = 400$ and 600 nm rather than at $X_s = 0.5D$. According to Figs. 4, 6, 8, the lateral shift for the minimum heat flux is relevant to the grating period $D$, chemical potential $\mu$, and the filling fraction $f$. Considering that both the scale of the lateral shift and the geometry, considered here, are realistic and experimentally accessible, the lateral-displacement-sensitive radiative heat transfer might have potential for thermal logic gates applications.

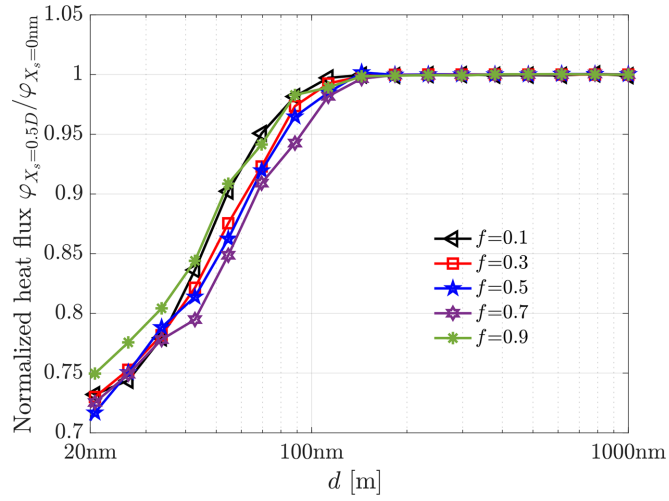


FIG. 9. Dependence of normalized heat flux $\varphi_{X_s=0.5D}/\varphi_{X_s=0\,\text{nm}}$ on separation distance $d$. Five different filling fractions are considered, $f = 0.1$, 0.3, 0.5, 0.7, and 0.9, respectively. The grating period $D = 100$ nm, chemical potential $\mu = 0.5$ eV.

### B. Asymptotic regimes for the LSE on NFRHT

In this section, we try to find an asymptotic regime map for the LSE on NFRHT between substrate-supported graphene gratings to quickly tell the existence of the LSE or not. Considering that the relevance of the dimensionless geometric factor $d/D$ for the LSE has been confirmed in Sec. III A, we may take advantage of it to propose the asymptotic regime map. That is, as the filling fraction $f$ approaches 0 or 1, the LSE disappears. Hereinafter, we will use the ratio of heat flux with a half-period shift $\varphi(X_s = 0.5D)$ to that without a shift $\varphi(X_s = 0)$ to evaluate the LSE on heat flux.

We will, first, check whether the filling fraction affects the asymptotic regime. The dependence of the ratio $\varphi(X_s = 0.5D)/\varphi(X_s = 0)$ on the separation distance $d$ is shown in Fig. 9, where five different filling fractions are considered: $f = 0.1$, 0.3, 0.5, 0.7, and 0.9. The grating period is $D = 100$ nm, and the chemical potential is $\mu = 0.5$ eV. We can see a clear dependance of the ratio $\varphi(X_s = 0.5D)/\varphi(X_s = 0)$ on $d$ with two distinct regime zones: (i) the first one for $d \leqslant 200$ nm, where the ratio varies quickly, and (ii) the second one for $d \geqslant 200$ nm, where the ratio is almost constant. Moreover, we remark that, even for small period configurations (i.e., 100 nm), the lateral shift can still have a wide range modulation of the heat flux, with a maximum reduction of 30% (in the first zone).

Beyond the separation point $d = 200$ nm, the LSE becomes less important. In addition, such a critical separation point does not change with the filling fraction $f$. To understand why the LSE on heat transfer changes with the separation $d$, we show the energy transmission coefficient $\text{Tr}(\mathcal{O})$ in the $(k_x/k_0,\ k_y/k_0)$ plane at the angular frequency $\omega = 5 \times 10^{13}$rad/s (where the contribution of graphene to the NFRHT spectrum is important) for a slab coated with a graphene grating in Fig. 10. Here, $\text{Tr}(\mathcal{O})$ is the sum over the two polarizations of the photon tunneling probabilities, which is usually applied to analyze the mechanisms behind NFRHT [45,60,61]. The transmission coefficient operator $\mathcal{O}$ is defined

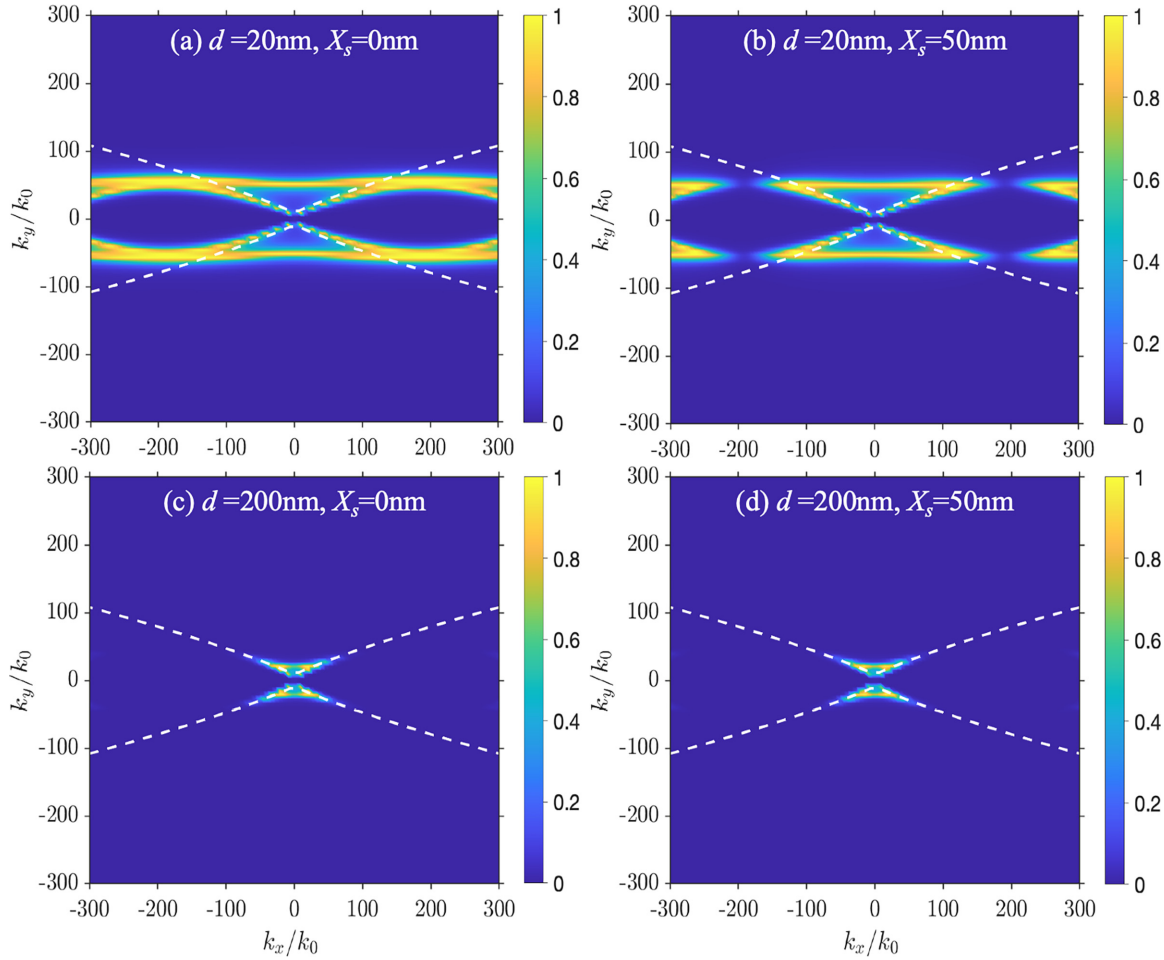


FIG. 10. Energy transmission coefficient for a fused silica substrate coated with a graphene grating: (a) separation $d = 20$ nm and lateral shift $X_s = 0$ nm, (b) separation $d = 20$ nm and lateral shift $X_s = 50$ nm, (c) separation $d = 200$ nm and lateral shift $X_s = 0$ nm, and (d) separation $d = 200$ nm and lateral shift $X_s = 50$ nm. The grating period $D = 100$ nm, chemical potential $\mu = 0.5$ eV, filling fraction $f = 0.5$.

by Eq. (4). In Fig. 10, four configurations are considered: (a) $d = 20$ nm and $X_s = 0$ nm, (b) $d = 20$ nm and $X_s = 50$ nm, (c) $d = 200$ nm and $X_s = 0$ nm, and (d) $d = 200$ nm and $X_s = 50$ nm, together with $D = 100$ nm, $\mu = 0.5$ eV, and $f = 0.5$. The dotted curves represent the dispersion relations obtained from the poles of the reflection coefficient [49,62].

For the configurations with $d = 200$ nm, the topology of the accessible modes does not change with the lateral shift, as shown in Figs. 10(c) and 10(d). However, for $d = 20$ nm, the topology of the accessible modes changes slightly, as shown in Figs. 10(a) and 10(b). There are more accessible high-$k$ modes for the case with no lateral shift than that for the case with a half-period lateral shift, which accounts for the fact that the radiative heat flux decreases significantly as the upper body 2 moves from the aligned situation to the misaligned one. Whether or not the lateral shift exists, the supported surface plasmon polariton is always the hyperbolic one. Compared with the transition from the circular one to the hyperbolic one by patterning the graphene sheet into a grating, the lateral shift will not induce a critical topology transition but only slightly affect the accessible range of high-$k$ modes.

Now we investigate and determine the asymptotic regime map for the LSE by using the geometric factor $d/D$. For that, we take the typical filling fraction $f = 0.5$ and chemical potential $\mu = 0.5$ eV. In Fig. 11, we show the ratio $\varphi_{X_s=0.5D}/\varphi_{X_s=0\,\mathrm{nm}}$ in the $(d, D)$ plane, where the black dotted lines corresponding to the lines representing the geometric factors $d/D = 0.5$, 1.0, and 2.0 are added for reference.

For a given grating period $D$, as the separation $d$ becomes large enough, the ratio $\varphi_{X_s=0.5D}/\varphi_{X_s=0\,\mathrm{nm}}$ approaches 1, and the scattering details of the graphene grating no longer change with the relative lateral shift $X_s$. That is, the two graphene gratings see each other as an effective whole rather than in detail, and thus, the LSE on heat transfer becomes less important.

Additionally, for a fixed separation $d$, as the period $D$ decreases, the ratio $\varphi_{X_s=0.5D}/\varphi_{X_s=0\,\mathrm{nm}}$ also approaches 1 gradually, and the scattering details of the graphene grating no longer change with the relative lateral shift $X_s$. When the grating period $D$ is relatively small compared with the separation $d$, the graphene grating behaves like an effective medium, and the relative lateral shift between the two gratings does not change the scattering details and thus does not affect the heat

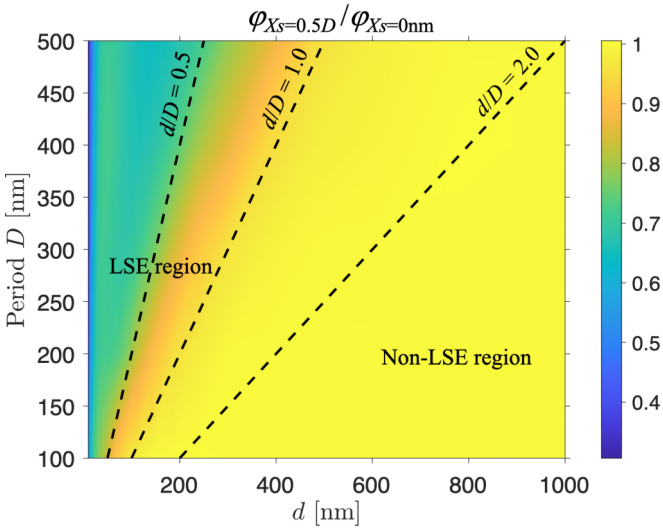


FIG. 11. Dependence of the ratio $\varphi_{X_s=0.5D}/\varphi_{X_s=0\,\mathrm{nm}}$ on separation distance $d$ and grating period $D$. The filling fraction $f = 0.5$, chemical potential $\mu = 0.5\,\mathrm{eV}$. The dotted lines (geometric factor $d/D = 0.5$, 1.0, and 2.0, respectively) are added for reference.

transfer. We can clearly see that the ratio $\varphi_{X_s=0.5D}/\varphi_{X_s=0\,\mathrm{nm}}$ generally increases to 1 as the geometric factor $d/D$ increases. The LSE on heat transfer becomes less and less important as $d/D$ increases. Two distinct regions can be distinguished, where we see a significant LSE and a negligible LSE on heat transfer, respectively (namely, the LSE and non-LSE regions). In the LSE region, the lateral shift can even result in >50% reduction of the heat flux. For clarity, we take several lines ($D = 100$, 200, 300, 400, and 500 nm) from Fig. 11 and show them in Fig. 12 to follow the details of the the dependence of the ratio $\varphi_{X_s=0.5D}/\varphi_{X_s=0\,\mathrm{nm}}$ on the separation $d$. The inset in

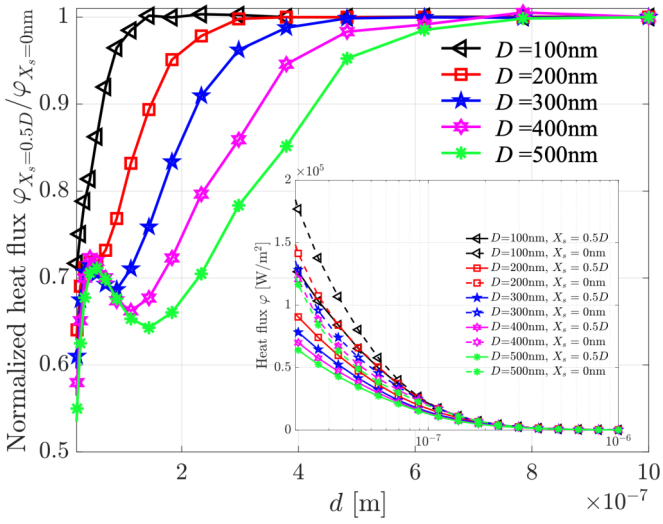


FIG. 12. Dependence of the ratio $\varphi_{X_s=0.5D}/\varphi_{X_s=0\,\mathrm{nm}}$ (main figure) and the heat flux $\varphi$ (inset) on separation distance $d$ for five different grating periods, $D = 100$, 200, 300, 400, and 500 nm. The filling fraction $f = 0.5$, chemical potential $\mu = 0.5\,\mathrm{eV}$.

Fig. 12 is for the dependence of the absolute heat flux on the separation $d$.

Although the heat flux $\varphi$ decreases monotonically with the separation $d$ for both $X_s = 0$ nm and $X_s = 0.5D$, the ratio $\varphi_{X_s=0.5D}/\varphi_{X_s=0\,\mathrm{nm}}$ is usually not monotonic with this separation $d$. The dependence of heat flux $\varphi$ on $d$ is not synchronized for the two configurations with lateral shift $X_s = 0$ nm and $X_s = 0.5D$. For the gratings with the same filling fraction $f$, as the separation $d$ increases to 200 nm or more, they always have the same heat flux, even though they have different periods $D$. That is, for two gratings with a large enough separation, it is the filling fraction that plays the determining role for the heat transfer rather than the grating period.

To understand the separation-dependent shift effect on the heat flux, we show its spectrum for two separations ($d = 20$ and 50 nm) in Fig. 13. Two relative shifts are considered, $X_s = 0$ nm and $X_s = 0.5D$ with $D = 500$ nm, $f = 0.5$, and $\mu = 0.5\,\mathrm{eV}$. The spectra for the configurations of bare slabs and slabs coated with graphene sheets are also added for reference. The graphene coating (including the graphene grating and the graphene sheet) increases the whole heat flux spectrum apart from the peaks. As compared with the graphene grating coating, the graphene sheet coating can induce a reduction of the low-frequency (at $\sim 9 \times 10^{13}$ rad/s) peak and a redshift of the high-frequency (at $\sim 2 \times 10^{14}$ rad/s) peak. The lateral shift between the two objects reduces the whole spectrum of heat flux from the dashed blue line to the red solid line (as shown in Fig. 13). The difference between the red and blue line spectra is more pronounced for small $d$.

To further understand the observations concerning the separation-dependent LSE on the radiative heat transfer in Figs. 11 and 12, we show the energy transmission coefficient $\mathrm{Tr}(\mathcal{O})$ [see Eq. (4) for the definition] in the ($k_x/k_0$, $k_y/k_0$) plane at the angular frequency $\omega = 5 \times 10^{13}$ rad/s for a slab coated with a graphene grating in Fig. 14. Eight configurations are considered, where the upper panels [(a)–(d)] are for the configurations without a lateral shift (i.e., $X_s = 0$ nm), and the lower panels [(e)–(h)] are for configurations with a fixed half-period lateral shift (i.e., $X_s = 0.5D = 250$ nm). The separations $d = 20$, 200, 400, and 600 nm are considered, while $D = 500$ nm, $\mu = 0.5\,\mathrm{eV}$, and $f = 0.5$. The dotted curves represent the dispersion relations obtained from the poles of the reflection coefficient [49,62].

When increasing the separation $d$, by comparing the panels [(a)–(d)] with panels [(e)–(h)] correspondingly in Fig. 14, we show that the difference between the topologies of the allowed modes caused by the relative lateral shift becomes less and less important. In addition, we can see in Fig. 14(a) a shrinking region for the allowed modes as the separation $d$ increases, regardless of whether there is a lateral shift, which results in a decreasing heat flux. Particularly, at separation $d = 20$ nm, the high-$k$ branch allowed modes blend and hybridize significantly with the relative low-$k$ branch due to the difference in the near field caused by the lateral shift. The near-field effect weakens with the mismatch between the two objects. Hence, less energy can be exchanged between the two objects due to the lateral shift at short separation. A general conclusion is that the lateral shift works against the radiative heat transfer for short separations but becomes less important for large separations.

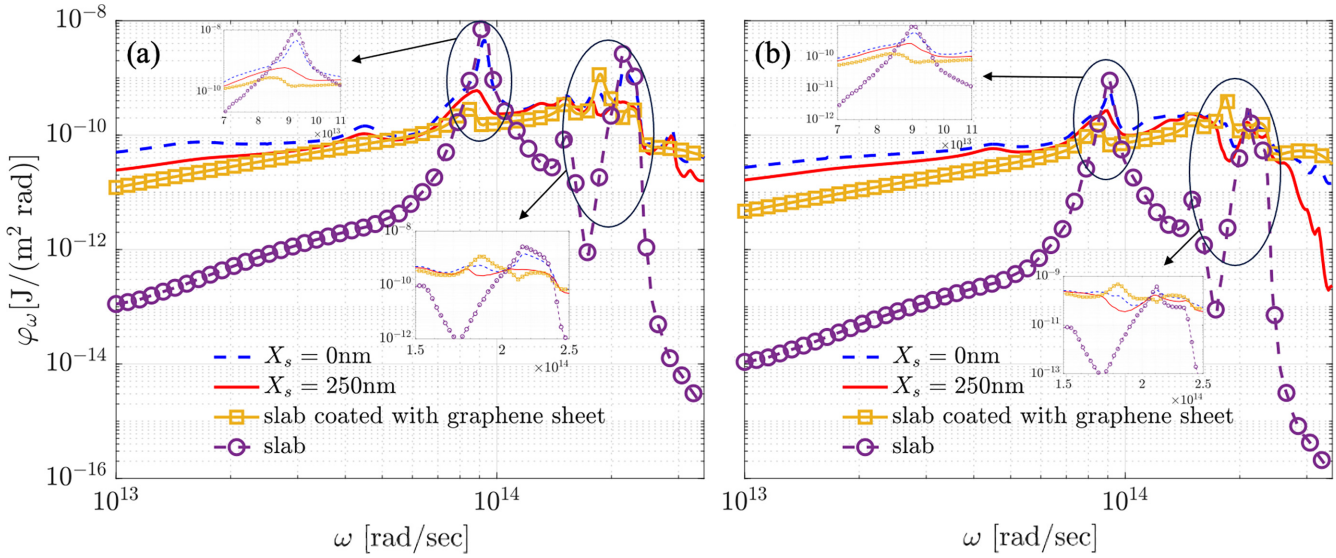


FIG. 13. Spectra of heat flux between two objects with two relative shifts ($X_s = 0$ nm and $0.5D$) and two different separations: (a) separation $d = 20$ nm and (b) separation $d = 50$ nm. The grating period $D = 500$ nm, filling fraction $f = 0.5$, chemical potential $\mu = 0.5$ eV. The heat flux spectra for the configurations of bare slabs and slabs coated with graphene sheets are also added for reference.

## IV. CONCLUSIONS

We analyzed theoretically the effect of a lateral shift on NFRHT between finite-thickness planar fused silica slabs coated with graphene gratings, through FMM-LBF. Compared with the effective medium approximation, which treats the grating as an effective whole rather than in detail, this more accurate approach goes far beyond, especially because the former cannot account for the lateral shift. To consider the lateral shift in the FMM-LBF and in addition to the existing method of including the lateral shift by directly applying the reference translation to the scattering operators [58], we developed another method to include the LSE in the scattering operators themselves.

We show that, due to the lateral shift, the heat flux can exhibit significant oscillations and even a 60–70% reduction compared with the aligned case (e.g., $f = 0.2$, $\mu = 0.5$ eV, $D = 1000$ nm, $d = 100$ nm). Such a LSE is found to be sensitive to the geometric factor $d/D$. If $d/D < 0.5$ (see

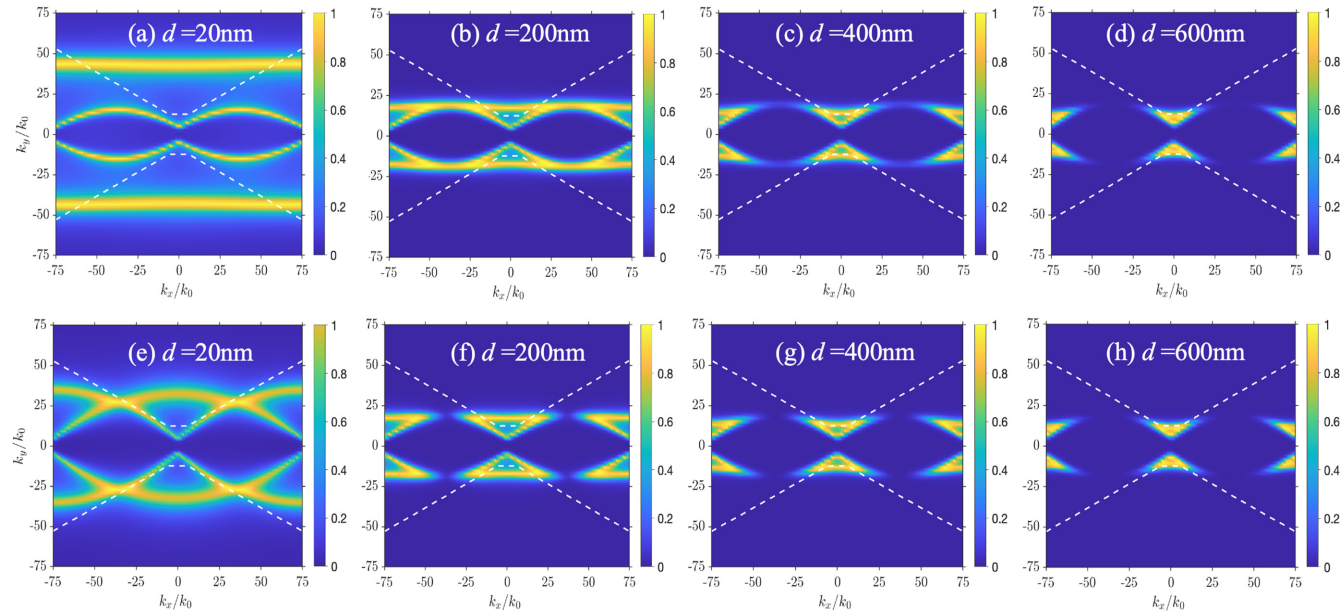


FIG. 14. Energy transmission coefficient for a fused silica substrate coated with a graphene grating: (a) separation $d = 20$ nm and lateral shift $X_s = 0$ nm, (b) separation $d = 200$ nm and lateral shift $X_s = 0$ nm, (c) separation $d = 400$ nm and lateral shift $X_s = 0$ nm, (d) separation $d = 600$ nm and lateral shift $X_s = 0$ nm, (e) separation $d = 20$ nm and lateral shift $X_s = 250$ nm, (f) separation $d = 200$ nm and lateral shift $X_s = 250$ nm, (g) separation $d = 400$ nm and lateral shift $X_s = 250$ nm, and (h) separation $d = 600$ nm and lateral shift $X_s = 250$ nm. The grating period $D = 500$ nm, chemical potential $\mu = 0.5$ eV, filling fraction $f = 0.5$.

Fig. 11 for the regime map of the LSE), the ratio of the heat flux with a half-period shift to that without a shift ($\varphi_{X_s=0.5D}/\varphi_{X_s=0\,\mathrm{nm}}$) is far from unity. That is, the lateral shift significantly reduces the heat flux. However, we can generally say that, when $d/D > 1$, the ratio $\varphi_{X_s=0.5D}/\varphi_{X_s=0\,\mathrm{nm}} \sim 1$ (see Figs. 5 and 11), where the LSE on heat transfer becomes less important. We can clearly distinguish two asymptotic regimes for the radiative heat transfer, i.e., the LSE and non-LSE regimes, where we see a significant LSE and a negligible LSE on heat transfer, respectively.

Regardless of the lateral shift, the radiative heat flux shows a nonmonotonic dependence on the graphene chemical potential, with the heat flux reaching its maximum value at $\mu \approx 0.25$ eV. Considering that all the length scales (e.g., the lateral shift and the period) are realistic and experimentally accessible, the lateral-shift-sensitive and chemical-potential-dependent radiative heat transfer might have potential for the thermal logic gate. It would also be interesting to study the effect of the lateral shift of the grating on Casimir interactions [63,64].

## ACKNOWLEDGMENTS

This paper was supported by CAT (Grant No. A-HKUST604/20) from the ANR/RGC Joint Research Scheme sponsored by the French National Research Agency (ANR) and the Research Grants Council (RGC) of the Hong Kong Special Administrative Region, China.

## APPENDIX: MODIFIED FMM-LBF WITH A LATERAL SHIFT

The main text outlined two distinct approaches to compute the scattering matrix of our structure. In the first approach, the lateral shift is directly incorporated into the scattering matrix elements [as presented in Eq. (8)]. In contrast, the second approach requires a modification of the FMM-LBF method itself. This Appendix is dedicated to a detailed derivation of the latter approach.

In our recent work [53], we provided comprehensive details of FMM-LBF with no lateral shift ($X_s = 0$). In this context, we initially computed the interface scattering matrix $S_{\mathrm{LBF}}$ between the input media I and II (as shown in Fig. 2). Then we determined the slab scattering matrix, denoted $S_{\mathrm{slab}}$, between media II and III. By performing the star product ($\star$) operation [53] between $S_{\mathrm{LBF}}$ and $S_{\mathrm{slab}}$, we obtained the overall scattering matrix, denoted $S$ and given by

$$S = S_{\mathrm{LBF}} \star S_{\mathrm{slab}} = \begin{pmatrix} \mathcal{R}^{-}_{xyz} & \mathcal{T}^{-}_{xyz} \\ \mathcal{T}^{+}_{xyz} & \mathcal{R}^{+}_{xyz} \end{pmatrix}, \tag{A1}$$

where $\mathcal{R}^{+}_{xyz}$ and $\mathcal{R}^{-}_{xyz}$ ($\mathcal{T}^{+}_{xyz}$ and $\mathcal{T}^{-}_{xyz}$) are the reflection operators (transmission operators) in the $(x, y, z)$ Cartesian basis.

In the presence of a lateral shift $X_s$, as illustrated in Fig. 2, the definition of the matrix $S_{\mathrm{LBF}}$ is modified, while the rest of the calculation process remains the same. Let us proceed to compute this new matrix.

Due to periodicity along the $x$ direction, new diffraction channels open up, characterized by the wave vector component in that direction. The $z$ component of the $n$th diffraction-order wave vector depends on the medium. Here, $k^{\mathrm{I}}_{zn}$ and $k^{\mathrm{II}}_{zn}$ represent the $z$ wave vector of the $n$th diffraction order for media I (with $\varepsilon_{\mathrm{I}}$ on the incidence side) and II (with $\varepsilon_{\mathrm{II}}$ on the output side), respectively, and are given by

$$\begin{aligned} k^{\mathrm{I}}_{zn} &= \sqrt{k_0^2\varepsilon_{\mathrm{I}} - k_{xn}^2 - k_y^2}, \\ k^{\mathrm{II}}_{zn} &= \sqrt{k_0^2\varepsilon_{\mathrm{II}} - k_{xn}^2 - k_y^2}, \end{aligned} \tag{A2}$$

with $k_0 = \omega/c$, $k_{xn} = k_x + n\frac{2\pi}{D}$, $k_x$ is in the first Brillouin zone $(-\frac{\pi}{D}, \frac{\pi}{D})$, and $k_y$ is in $\mathbb{R}$.

The electric and magnetic fields in medium I can be expressed as

$$\begin{aligned} \mathbf{E}_{\mathrm{I}} &= \sum_n [\mathbf{I}_n \exp(i\mathbf{k}_{\mathrm{i}n}\cdot\mathbf{r}) + \mathbf{R}_n \exp(i\mathbf{k}_{\mathrm{r}n}\cdot\mathbf{r})], \\ \mathbf{H}_{\mathrm{I}} &= \frac{1}{k_0 Z_0}\sum_n [\mathbf{k}_{\mathrm{i}n}\times\mathbf{I}_n \exp(i\mathbf{k}_{\mathrm{i}n}\cdot\mathbf{r}) + \mathbf{k}_{\mathrm{r}n}\times\mathbf{R}_n \exp(i\mathbf{k}_{\mathrm{r}n}\cdot\mathbf{r})], \end{aligned} \tag{A3}$$

Here, $\mathbf{I}_n = (I_{xn}, I_{yn}, I_{zn})$, $\mathbf{R}_n = (R_{xn}, R_{yn}, R_{zn})$, $\mathbf{k}_{\mathrm{i}n} = (k_{xn}, k_y, k^{\mathrm{I}}_{zn})$, $\mathbf{k}_{\mathrm{r}n} = (k_{xn}, k_y, -k^{\mathrm{I}}_{zn})$, and $Z_0 = \sqrt{\frac{\mu_0}{\varepsilon_0}}$, with $n \in \mathbb{Z}$. Typically, in the numerical implementation, we retain only $2N+1$ Fourier coefficients, i.e., $n \in [-N, N]$, where $N$ is called the truncation order.

In medium II, the electric and magnetic fields are

$$\begin{aligned} \mathbf{E}_{\mathrm{II}} &= \sum_n [\mathbf{T}_n \exp(i\mathbf{k}_{\mathrm{t}n}\cdot\mathbf{r}) + \mathbf{I}'_n \exp(i\mathbf{k}_{\mathrm{i}'n}\cdot\mathbf{r})], \\ \mathbf{H}_{\mathrm{II}} &= \frac{1}{k_0 Z_0}\sum_n [\mathbf{k}_{\mathrm{t}n}\times\mathbf{T}_n \exp(i\mathbf{k}_{\mathrm{t}n}\cdot\mathbf{r}) + \mathbf{k}_{\mathrm{i}'n}\times\mathbf{I}'_n \exp(i\mathbf{k}_{\mathrm{i}'n}\cdot\mathbf{r})], \end{aligned} \tag{A4}$$

where $\mathbf{T}_n = (T_{xn}, T_{yn}, T_{zn})$, $\mathbf{I}'_n = (I'_{xn}, I'_{yn}, I'_{zn})$, $\mathbf{k}_{\mathrm{t}n} = (k_{xn}, k_y, k^{\mathrm{II}}_{zn})$, and $\mathbf{k}_{\mathrm{i}'n} = (k_{xn}, k_y, -k^{\mathrm{II}}_{zn})$.

Furthermore, using div$\mathbf{E} = \mathbf{k}\cdot\mathbf{E} = 0$, we have the following relations

$$\begin{aligned} I_{zn} &= -\frac{1}{k_{zn}^{\mathrm{I}}}(k_{xn}I_{xn} + k_y I_{yn}), \\ R_{zn} &= \frac{1}{k_{zn}^{\mathrm{I}}}(k_{xn}R_{xn} + k_y R_{yn}), \\ T_{zn} &= -\frac{1}{k_{zn}^{\mathrm{II}}}(k_{xn}T_{xn} + k_y T_{yn}), \\ I'_{zn} &= \frac{1}{k_{zn}^{\mathrm{II}}}(k_{xn}I'_{xn} + k_y I'_{yn}). \end{aligned} \tag{A5}$$

The boundary conditions for the electric field at $z = 0$ are

$$\begin{aligned} E_{\mathrm{I}x}(x, y, 0) &= E_{\mathrm{II}x}(x, y, 0), \\ E_{\mathrm{I}y}(x, y, 0) &= E_{\mathrm{II}y}(x, y, 0). \end{aligned} \tag{A6}$$

By inserting Eqs. (A3) and (A4) into Eq. (A6), for arbitrary $n$, we have

$$\begin{aligned} I_{xn} + R_{xn} &= I'_{xn} + T_{xn}, \\ I_{yn} + R_{yn} &= I'_{yn} + T_{yn}, \end{aligned} \tag{A7}$$

which can be expressed in compact form:

$$I + R = I' + T, \tag{A8}$$

where

$$I = \begin{pmatrix} I_x \\ I_y \end{pmatrix}, \quad R = \begin{pmatrix} R_x \\ R_y \end{pmatrix}, \quad I' = \begin{pmatrix} I'_x \\ I'_y \end{pmatrix}, \quad T = \begin{pmatrix} T_x \\ T_y \end{pmatrix}. \tag{A9}$$

Due to the zero-thickness approximation of the graphene grating, the boundary conditions for the magnetic fields at the interface between media I and II are

$$H_{\mathrm{II}x}(x, y, 0) - H_{\mathrm{I}x}(x, y, 0) = \sigma(x)E_{\mathrm{II}y}(x, y, 0), \tag{A10}$$

where the function $\sigma(x)$ is periodic and can be expanded into Fourier series as follows:

$$\sigma(x) = \begin{cases} \sigma_g, & \text{if } X_s < x < X_s + a \text{ (graphene)}, \\ 0, & \text{if } X_s + a < x < X_s + D \text{ (slit)}, \end{cases} = \sum_n \sigma_n \exp\left(i\frac{2\pi}{D}nx\right). \tag{A11}$$

By inserting Eqs. (A3) and (A4) into Eq. (A10), and using the Laurent factorization rule, the following relation is obtained:

$$\left\{\left(k_y T_{zn} - k_{zn}^{\mathrm{II}}T_{yn}\right) + \left(k_y I'_{zn} + k_{zn}^{\mathrm{II}}I'_{yn}\right) - \left(k_y I_{zn} - k_{zn}^{\mathrm{I}}I_{yn}\right) - \left(k_y R_{zn} + k_{zn}^{\mathrm{I}}R_{yn}\right)\right\} = k_0 Z_0 \sum_{n'}\left\{\sigma_{n'-n}\left(T_{yn'} + I'_{yn'}\right)\right\}. \tag{A12}$$

That can be expressed in a compact matrix form as

$$(k_y T_z - \gamma_{\mathrm{II}}T_y) + \left(k_y I'_z + \gamma_{\mathrm{II}}I'_y\right) - (k_y I_z - \gamma_{\mathrm{I}}I_y) - (k_y R_z + \gamma_{\mathrm{I}}R_y) = k_0 Z_0 [[\sigma]](T_y + I'_y), \tag{A13}$$

where $\gamma_{\mathrm{II}} = \mathrm{diag}(k_{zn}^{\mathrm{II}})$, $\gamma_{\mathrm{I}} = \mathrm{diag}(k_{zn}^{\mathrm{I}})$, and $[[\sigma]]$ is the Toeplitz matrix whose $(n', n)$ element is $\sigma_{n'-n}$; more precisely,

$$[[\sigma]] = \begin{pmatrix} \sigma_0 & \sigma_{-1} & & & \sigma_{-2N} \\ \sigma_1 & \sigma_0 & \sigma_{-1} & & \\ & \ddots & \ddots & \ddots & \\ & & \ddots & \ddots & \sigma_{-1} \\ \sigma_{2N} & & & \sigma_1 & \sigma_0 \end{pmatrix}, \tag{A14}$$

where $\sigma_p = \frac{i\sigma_g}{2\pi p}\exp(-\frac{i2\pi pX_s}{D})[\exp(-\frac{i2\pi pa}{D}) - 1] = \exp(-\frac{i2\pi pX_s}{D})\overline{\sigma}_p$ when $p$ is a nonzero integer, $\sigma_0 = \sigma_g a/D = \overline{\sigma}_0$, and $\overline{\sigma}_p$ and $\overline{\sigma}_0$ correspond to the case $X_s = 0$ [51,53].

In addition, when considering a lateral translation $X_s$, the electric field $E_x$ on the graphene grating surface ($z = 0$) can be expressed in terms of LBFs [$g'_m(x)$ and $s'_m(x)$] as follows:

$$E_x(x, y) = \exp(ik_y y)\begin{cases} \sum_{m=1}^{N_g} p_m g'_m(x), & \text{if } X_s < x < X_s + a, \\ \sum_{m=0}^{N_s-1} q_m s'_m(x), & \text{if } X_s + a < x < X_s + D, \end{cases} \tag{A15}$$

where

$$g_m(x) = \sin(m\pi x/a),$$
$$s_m(x) = \frac{\cos[m\pi(x-a)/c']}{\sqrt{(c'/2)^2-(x-x_c)^2}}, \tag{A16}$$

with $c' = D - a$, $x_c = (a + D)/2$, $N_g = \text{round}[\frac{N\times a}{D}]$, $N_s = N - N_g$, and round$(x)$ gives the nearest integer number, then

$$g'_m(x) = g_m(x - X_s), \quad \text{if } X_s < x < X_s + a,$$
$$s'_m(x) = s_m(x - X_s), \quad \text{if } X_s + a < x < X_s + D. \tag{A17}$$

Projecting the boundary condition for the $y$ component of the magnetic field on the $[\exp(-ik_{xn}x)]$ basis, we obtain

$$\left(k^{\text{II}}_{zn}T_{xn} - k_{xn}T_{zn} - k^{\text{II}}_{zn}I'_{xn} - k_{xn}I'_{zn}\right) - \left(k^{\text{I}}_{zn}I_{xn} - k_{xn}I_{zn} - k^{\text{I}}_{zn}R_{xn} - k_{xn}R_{zn}\right) = -\sigma_g k_0 Z_0 \sum_{m=1}^{N_g} \langle \exp(-ik_{xn}x),\, p_m g'_m(x)\rangle, \tag{A18}$$

where the scalar product is given by $\langle f, g\rangle = \frac{1}{D}\int_{X_s}^{X_s+D} f(x)g(x)dx$. Then Eq. (A18) yields

$$\left(k^{\text{II}}_{zn}T_{xn} - k_{xn}T_{zn} - k^{\text{II}}_{zn}I'_{xn} - k_{xn}I'_{zn}\right) - \left(k^{\text{I}}_{zn}I_{xn} - k_{xn}I_{zn} - k^{\text{I}}_{zn}R_{xn} - k_{xn}R_{zn}\right)$$
$$= -\frac{1}{D}\int_{X_s}^{X_s+a} \sigma_g k_0 Z_0 \sum_{m=1}^{N_g} p_m g_m(x - X_s)\exp(-ik_{xn}x)dx. \tag{A19}$$

Using the change of variable $x' = x - X_s$, Eq. (A19) becomes

$$\left(k^{\text{II}}_{zn}T_{xn} - k_{xn}T_{zn} - k^{\text{II}}_{zn}I'_{xn} - k_{xn}I'_{zn}\right) - \left(k^{\text{I}}_{zn}I_{xn} - k_{xn}I_{zn} - k^{\text{I}}_{zn}R_{xn} - k_{xn}R_{zn}\right)$$
$$= -\frac{1}{D}\int_{0}^{a} \sigma_g k_0 Z_0 \sum_{m=1}^{N_g} p_m g_m(x')\exp(-ik_{xn}x' - ik_{xn}X_s)dx'. \tag{A20}$$

By taking out the term $\exp(-ik_{xn}X_s)$ in the integral and exchanging the order of summation and integration, the right-hand side of Eq. (A20) becomes

$$-\frac{1}{D}\int_{0}^{a} \sigma_g k_0 Z_0 \sum_{m=1}^{N_g} p_m g_m(x')\exp\left(-ik_{xn}x' - ik_{xn}X_s\right)dx' = -\sigma_g k_0 Z_0 \exp(-ik_{xn}X_s)\sum_{m=1}^{N_g} p_m G_{nm}, \tag{A21}$$

where $G_{nm} = \frac{-ia}{2D}\exp(-ik_{xn}a/2)[\exp(im\pi/2)\sin c(\alpha^-_{nm}a/2) - \exp(-im\pi/2)\sin c(\alpha^+_{nm}a/2)]$, and $\alpha^{\pm}_{nm} = m\pi/a \pm k_{xn}$.

Equation (A19) can now be recast into a more compact form:

$$\gamma_{\text{II}}T_x - \alpha T_z - \gamma_{\text{II}}I'_x - \alpha I'_z - \gamma_1 I_x + \alpha I_z + \gamma_1 R_x + \alpha R_z = -\sigma_g k_0 Z_0 \Delta \mathbb{G} p, \tag{A22}$$

where $\alpha = \text{diag}(k_{xn})$, $\Delta = \text{diag}[\exp(-ik_{xn}X_s)]$, $\mathbb{G} = \{G_{nm}\}$ is a matrix with size $[(2N + 1) \times N_g]$, and $p$ is the column vector formed by the $N_g$ coefficients $p_m$, with $p = (p_1, p_2, p_3, \ldots, p_{N_g})^{\text{T}}$. We can write the above equation as follows:

$$\gamma_{\text{II}}T_x - \alpha T_z - \gamma_{\text{II}}I'_x - \alpha I'_z - \gamma_1 I_x + \alpha I_z + \gamma_1 R_x + \alpha R_z = -\sigma_g k_0 Z_0 [\Delta\mathbb{G}\ \mathbf{0}]\begin{pmatrix} p \\ q \end{pmatrix}, \tag{A23}$$

where $[\Delta\mathbb{G}\ \mathbf{0}]$ is the horizontale concatenation of matrices $\Delta\mathbb{G}$ and $\mathbf{0}$, denoting the zero matrix of size $[(2N + 1) \times N_s]$, and $q$ is the column vector formed by the $N_s$ coefficients $q_m$, with $q = (q_0, q_1, q_2, \ldots, q_{N_s-1})^{\text{T}}$.

To obtain $(p, q)^{\text{T}}$, we use the boundary condition on the $x$ component of the electric field, and following the same procedure as that for the $y$ component of the magnetic field, we obtain

$$\begin{pmatrix} p \\ q \end{pmatrix} = [\Delta\mathbb{G}\ \Delta\mathbb{S}]^{-1}\left(T_x + I'_x\right), \tag{A24}$$

where $[\Delta\mathbb{G}\ \Delta\mathbb{S}]$ is the horizontale concatenation of matrices $\Delta\mathbb{G}$ and $\Delta\mathbb{S}$, $S_{nm} = \frac{\pi}{2D}\exp(-ik_{xn}x_c)[\exp(im\pi/2)J_0(\beta^-_{nm}c'/2) + \exp(-im\pi/2)J_0(\beta^+_{nm}c'/2)]$, $\beta^{\pm}_{nm} = m\pi/c' \pm k_{xn}$, and $J_0(x)$ is the zero-order Bessel function of the first kind.

Finally, the modified interface scattering matrix $S_{\text{LBF}}$ is given by

$$\begin{pmatrix} R \\ T \end{pmatrix} = S_{\text{LBF}}\begin{pmatrix} I \\ I' \end{pmatrix}, \tag{A25}$$

where

$$S_{\text{LBF}} = \begin{pmatrix} \mathbb{1} & -\mathbb{1} \\ B & A + \Lambda' \end{pmatrix}^{-1}\begin{pmatrix} -\mathbb{1} & \mathbb{1} \\ B & A - \Lambda' \end{pmatrix}, \tag{A26}$$

$\mathbb{1}$ being the identity matrix of size $[2(2N+1)\times 2(2N+1)]$, $\Lambda' = \mathrm{diag}(\sigma_g k_0 Z_0[\Delta\mathbb{G}\ \mathbf{0}][\Delta\mathbb{G}\ \Delta\mathbb{S}]^{-1}, [[\sigma]]k_0 Z_0)$, and $A$ and $B$ are defined as

$$A = \begin{pmatrix} \gamma_{\mathrm{II}} + \alpha^2\gamma_{\mathrm{II}}^{-1} & \alpha k_y \gamma_{\mathrm{II}}^{-1} \\ \alpha k_y \gamma_{\mathrm{II}}^{-1} & \gamma_{\mathrm{II}} + k_y^2 \gamma_{\mathrm{II}}^{-1} \end{pmatrix}, \tag{A27}$$

$$B = \begin{pmatrix} \gamma_{\mathrm{I}} + \alpha^2\gamma_{\mathrm{I}}^{-1} & \alpha k_y \gamma_{\mathrm{I}}^{-1} \\ \alpha k_y \gamma_{\mathrm{I}}^{-1} & \gamma_{\mathrm{I}} + k_y^2 \gamma_{\mathrm{I}}^{-1} \end{pmatrix}. \tag{A28}$$

As mentioned in the beginning of this Appendix, the remaining calculations necessary to obtain the scattering matrix of the global structure [i.e., the slab scattering matrix $S_{\mathrm{slab}}$ and the transformation matrices from the $(x, y, z)$ Cartesian basis to the (TE, TM) basis] proceed exactly as published in our previous work [53].


[1] S. M. Rytov, Y. A. Kravtsov, and V. I. Tatarskii, *Prinicples of Statistical Radiophysics 3: Elements of Random Fields* (Springer-Verlag, Berlin, 1989).

[2] D. Polder and M. Van Hove, Theory of radiative heat transfer between closely spaced bodies, Phys. Rev. B **4**, 3303 (1971).

[3] P. O. Chapuis, M. Laroche, S. Volz, and J.-J. Greffet, Near-field induction heating of metallic nanoparticles due to infrared magnetic dipole contribution, Phys. Rev. B **77**, 125402 (2008).

[4] A. Narayanaswamy and G. Chen, Thermal near-field radiative transfer between two spheres, Phys. Rev. B **77**, 075125 (2008).

[5] R. Carminati and J.-J. Greffet, Near-field effects in spatial coherence of thermal sources, Phys. Rev. Lett. **82**, 1660 (1999).

[6] J. J. Loomis and H. J. Maris, Theory of heat transfer by evanescent electromagnetic waves, Phys. Rev. B **50**, 18517 (1994).

[7] A. V. Shchegrov, K. Joulain, R. Carminati, and J.-J. Greffet, Near-field spectral effects due to electromagnetic surface excitations, Phys. Rev. Lett. **85**, 1548 (2000).

[8] A. I. Volokitin and B. N. J. Persson, Radiative heat transfer between nanostructures, Phys. Rev. B **63**, 205404 (2001).

[9] P. O. Chapuis, M. Laroche, S. Volz, and J.-J. Greffet, Radiative heat transfer between metallic nanoparticles, Appl. Phys. Lett. **92**, 201906 (2008).

[10] A. Manjavacas and F. J. García de Abajo, Radiative heat transfer between neighboring particles, Phys. Rev. B **86**, 075466 (2012).

[11] M. Nikbakht, Radiative heat transfer between core-shell nanoparticles, J. Quant. Spectrosc. Radiat. Transfer **221**, 164 (2018).

[12] R. Messina, S.-A. Biehs, and P. Ben-Abdallah, Surface-mode-assisted amplification of radiative heat transfer between nanoparticles, Phys. Rev. B **97**, 165437 (2018).

[13] J. Dong, J. M. Zhao, and L. H. Liu, Long-distance near-field energy transport via propagating surface waves, Phys. Rev. B **97**, 075422 (2018).

[14] Y. Zhang, H. L. Yi, H. P. Tan, and M. Antezza, Giant resonant radiative heat transfer between nanoparticles, Phys. Rev. B **100**, 134305 (2019).

[15] M. G. Luo, J. M. Zhao, L. H. Liu, and M. Antezza, Radiative heat transfer and radiative thermal energy for two-dimensional nanoparticle ensembles, Phys. Rev. B **102**, 024203 (2020).

[16] M. G. Luo, J. M. Zhao, and L. H. Liu, Heat diffusion in nanoparticle systems via near-field thermal photons, Int. J. Heat Mass Transf. **200**, 123544 (2023).

[17] S.-A. Biehs, F. S. S. Rosa, and P. Ben-Abdallah, Modulation of near-field heat transfer between two gratings, Appl. Phys. Lett. **98**, 243102 (2011).

[18] Y. H. Kan, C. Y. Zhao, and Z. M. Zhang, Near-field radiative heat transfer in three-body systems with periodic structures, Phys. Rev. B **99**, 035433 (2019).

[19] Y. Liu, F. Q. Chen, A. Caratenuto, Y. P. Tian, X. J. Liu, Y. T. Zhao, and Y. Zheng, Effective approximation method for nanogratings-induced near-field radiative heat transfer, Materials **15**, 998 (2022).

[20] S. Shen, A. Narayanaswamy, and G. Chen, Surface phonon polaritons mediated energy transfer between nanoscale gaps, Nano Lett. **9**, 2909 (2009).

[21] E. Rousseau, A. Siria, G. Jourdan, S. Volz, F. Comin, J. Chevrier, and J.-J. Greffet, Radiative heat transfer at the nanoscale, Nat. Photonics **3**, 514 (2009).

[22] R. S. Ottens, V. Quetschke, S. Wise, A. A. Alemi, R. Lundock, G. Mueller, D. H. Reitze, D. B. Tanner, and B. F. Whiting, Near-field radiative heat transfer between macroscopic planar surfaces, Phys. Rev. Lett. **107**, 014301 (2011).

[23] B. Song, Y. Ganjeh, S. Sadat, D. Thompson, A. Fiorino, V. Fernández-Hurtado, J. Feist, F. J. Garcia-Vidal, J. C. Cuevas, P. Reddy *et al.*, Enhancement of near-field radiative heat transfer using polar dielectric thin films, Nat. Nanotechnol. **10**, 253 (2015).

[24] M. Lim, S. S. Lee, and B. J. Lee, Near-field thermal radiation between doped silicon plates at nanoscale gaps, Phys. Rev. B **91**, 195136 (2015).

[25] J. I. Watjen, B. Zhao, and Z. M. Zhang, Near-field radiative heat transfer between doped-Si parallel plates separated by a spacing down to 200 nm, Appl. Phys. Lett. **109**, 203112 (2016).

[26] M. Ghashami, H. Geng, T. Kim, N. Iacopino, S. K. Cho, and K. Park, Precision measurement of phonon-polaritonic near-field energy transfer between macroscale planar structures under large thermal gradients, Phys. Rev. Lett. **120**, 175901 (2018).

[27] J. Yang, W. Du, Y. S. Su, Y. Fu, S. Gong, S. He, and Y. Ma, Observing of the super-Planckian near-field thermal radiation between graphene sheets, Nat. Commun. **9**, 4033 (2018).

[28] J. DeSutter, L. Tang, and M. Francoeur, A near-field radiative heat transfer device, Nat. Nanotechnol. **14**, 751 (2019).

[29] N. Iqbal, S. Zhang, S. Wang, Z. Fang, Y. Hu, Y. Dang, M. Zhang, Y. Jin, J. Xu, B. Ju *et al.*, Measuring near-field

radiative heat transfer in a graphene-SiC heterostructure, Phys. Rev. Appl. **19**, 024019 (2023).
[30] Y. Yang and L. Wang, Spectrally enhancing near-field radiative transfer between metallic gratings by exciting magnetic polaritons in nanometric vacuum gaps, Phys. Rev. Lett. **117**, 044301 (2016).
[31] R. Messina, A. Noto, B. Guizal, and M. Antezza, Radiative heat transfer between metallic gratings using Fourier modal method with adaptive spatial resolution, Phys. Rev. B **95**, 125404 (2017).
[32] G.-C. Cui, C.-L. Zhou, Y. Zhang, and H.-L. Yi, Significant enhancement of near-field radiative heat transfer by misaligned bilayer heterostructure of graphene-covered gratings, ASME J. Heat Mass Transfer **146**, 022801 (2024).
[33] V. B. Svetovoy, P. J. van Zwol, and J. Chevrier, Plasmon enhanced near-field radiative heat transfer for graphene covered dielectrics, Phys. Rev. B **85**, 155418 (2012).
[34] O. Ilic, M. Jablan, J. D. Joannopoulos, I. Celanovic, H. Buljan, and M. Soljačić, Near-field thermal radiation transfer controlled by plasmons in graphene, Phys. Rev. B **85**, 155422 (2012).
[35] Z. H. Zheng, X. L. Liu, A. Wang, and Y. M. Xuan, Graphene-assisted near-field radiative thermal rectifier based on phase transition of vanadium dioxide ($VO_2$), Int. J. Heat Mass Transf. **109**, 63 (2017).
[36] A. Volokitin, Casimir friction and near-field radiative heat transfer in graphene structures, Z. Naturforsch. A **72**, 171 (2017).
[37] B. Zhao, B. Guizal, Z. M. Zhang, S. Fan, and M. Antezza, Near-field heat transfer between graphene/hBN multilayers, Phys. Rev. B **95**, 245437 (2017).
[38] K. Z. Shi, Z. Y. Chen, X. Xu, J. Evans, and S. L. He, Optimized colossal near-field thermal radiation enabled by manipulating coupled plasmon polariton geometry, Adv. Mater. **33**, 2106097 (2021).
[39] R. Y. Liu, L. X. Ge, H. Y. Yu, Z. Cui, and X. H. Wu, Near-field radiative heat transfer via coupling graphene plasmons with different phonon polaritons in the reststrahlen bands, Eng. Sci. **18**, 224 (2022).
[40] L. Lu, B. Zhang, H. Ou, B. W. Li, K. Zhou, J. L. Song, Z. X. Luo, and Q. Cheng, Enhanced near-field radiative heat transfer between graphene/hBN systems, Small **18**, 2108032 (2022).
[41] J.-S. Wang and M. Antezza, Photon mediated energy, linear and angular momentum transport in fullerene and graphene systems beyond local equilibrium, Phys. Rev. B **109**, 125105 (2024).
[42] Y.-M. Zhang, M. Antezza, and J.-S. Wang, Controllable thermal radiation from twisted bilayer graphene, Int. J. Heat Mass Transf. **194**, 123076 (2022).
[43] X. L. Liu and Z. M. Zhang, Giant enhancement of nanoscale thermal radiation based on hyperbolic graphene plasmons, Appl. Phys. Lett. **107**, 143114 (2015).
[44] Y. Z. Hu, H. Li, Y. G. Zhu, and Y. Yang, Enhanced near-field radiative heat transport between graphene metasurfaces with symmetric nanopatterns, Phys. Rev. Appl. **14**, 044054 (2020).
[45] M. G. Luo, Y. Jeyar, B. Guizal, J. M. Zhao, and M. Antezza, Effect of graphene grating coating on near-field radiative heat transfer, Appl. Phys. Lett. **123**, 253902 (2023).
[46] M. J. He, H. Qi, Y. T. Ren, Y. Zhao, and M. Antezza, Active control of near-field radiative heat transfer by a graphene-gratings coating-twisting method, Opt. Lett. **45**, 2914 (2020).
[47] M. J. He, H. Qi, Y.-T. Ren, Y.-J. Zhao, and M. Antezza, Magnetoplasmonic manipulation of nanoscale thermal radiation using twisted graphene gratings, Int. J. Heat Mass Transf. **150**, 119305 (2020).
[48] M. G. Luo, J. M. Zhao, and M. Antezza, Near-field radiative heat transfer between twisted nanoparticle gratings, Appl. Phys. Lett. **117**, 053901 (2020).
[49] C.-L. Zhou, Y. Zhang, and H.-L. Yi, Enhancement and manipulation of near-field thermal radiation using hybrid hyperbolic polaritons, Langmuir **38**, 7689 (2022).
[50] B. Guizal and D. Felbacq, Electromagnetic beam diffraction by a finite strip grating, Opt. Commun. **165**, 1 (1999).
[51] R.-B. Hwang, Highly improved convergence approach incorporating edge conditions for scattering analysis of graphene gratings, Sci. Rep. **10**, 12855 (2020).
[52] Y. Jeyar, M. Antezza, and B. Guizal, Electromagnetic scattering by a partially graphene-coated dielectric cylinder: Efficient computation and multiple plasmonic resonances, Phys. Rev. E **107**, 025306 (2023).
[53] Y. Jeyar, M. G. Luo, K. Austry, B. Guizal, Y. Zheng, H. B. Chan, and M. Antezza, Tunable nonadditivity in the Casimir-Lifshitz force between graphene gratings, Phys. Rev. A **108**, 062811 (2023).
[54] L. A. Falkovsky and A. A. Varlamov, Space-time dispersion of graphene conductivity, Eur. Phys. J. B **56**, 281 (2007).
[55] L. A. Falkovsky, Optical properties of graphene, J. Phys.: Conf. Ser. **129**, 012004 (2008).
[56] S. A. Awan, A. Lombardo, A. Colli, G. Privitera, T. S. Kulmala, J. M. Kivioja, M. Koshino, and A. C. Ferrari, Transport conductivity of graphene at RF and microwave frequencies, 2D Mater. **3**, 015010 (2016).
[57] R. Messina and M. Antezza, Three-body radiative heat transfer and Casimir-Lifshitz force out of thermal equilibrium for arbitrary bodies, Phys. Rev. A **89**, 052104 (2014).
[58] R. Messina and M. Antezza, Scattering-matrix approach to Casimir-Lifshitz force and heat transfer out of thermal equilibrium between arbitrary bodies, Phys. Rev. A **84**, 042102 (2011).
[59] E. D. Palik, *Handbook of Optical Constants of Solids* (Academic, New York, 1998).
[60] R. Guérout, J. Lussange, F. S. S. Rosa, J.-P. Hugonin, D. A. R. Dalvit, J.-J. Greffet, A. Lambrecht, and S. Reynaud, Enhanced radiative heat transfer between nanostructured gold plates, Phys. Rev. B **85**, 180301(R) (2012).
[61] X. L. Liu and Z. M. Zhang, Graphene-assisted near-field radiative heat transfer between corrugated polar materials, Appl. Phys. Lett. **104**, 251911 (2014).
[62] C.-L. Zhou, Y. Zhang, Z. Torbatian, D. Novko, M. Antezza, and H.-L. Yi, Photon tunneling reconstitution in black phosphorus/hBN heterostructure, Phys. Rev. Mater. **6**, 075201 (2022).
[63] A. Noto, R. Messina, B. Guizal, and M. Antezza, Casimir-Lifshitz force out of thermal equilibrium between dielectric gratings, Phys. Rev. A **90**, 022120 (2014).
[64] M. Wang, L. Tang, C. Y. Ng, R. Messina, B. Guizal, J. A. Crosse, M. Antezza, C. T. Chan, and H. B. Chan, Strong geometry dependence of the Casimir force between interpenetrated rectangular gratings, Nat. Commun. **12**, 600 (2021).